ICES Journal of Marine Science Advance Access published May 12, 2015

ICES Journal of
Marine Science

ICES CIEM International Council for the Exploration of the Sea Conseil International pour l'Exploration de la Mer

ICES Journal of Marine Science; doi:10.1093/icesjms/fsv071

Numerical simulations of the competition between wind-driven mixing and surface heating in triggering spring phytoplankton blooms

Rica Mae Enriquez and John R. Taylor*

Department of Applied Mathematics and Theoretical Physics, University of Cambridge, Cambridge, Cambridgeshire CB3 0WA, UK

**Corresponding author: tel: +44 1223 337030; fax: +44 1223 765900; e-mail: j.r.taylor@damtp.cam.ac.uk*

Enriquez, R. M., and Taylor, J. R. Numerical simulations of the competition between wind-driven mixing and surface heating in triggering spring phytoplankton blooms. – ICES Journal of Marine Science, doi: 10.1093/icesjms/fsv071.

Received 4 August 2014; revised 18 March 2015; accepted 4 April 2015.

About 60 years ago, Sverdrup formalized the critical depth hypothesis to explain the timing of the spring phytoplankton bloom in terms of the depth of the surface mixed layer. In recent years, a number of refinements and alternatives to the critical depth hypothesis have been proposed, including the critical turbulence hypothesis which states that a bloom can occur when turbulent mixing is sufficiently weak, irrespective of the mixed layer depth. Here, we examine the relative influence of wind-driven mixing and net surface heating on phytoplankton growth. Of particular interest is whether wind-driven mixing can delay the spring bloom after winter convection gives way to net surface warming. We address these questions using high-resolution large-eddy simulations (LES) coupled with a simple phytoplankton model. We also describe an analytical phytoplankton model with a formulation for the turbulent mixing based on the LES results. For a constant, prescribed surface heat flux, net phytoplankton growth is seen when the windstress is smaller than a critical value. Similarly, for a constant windstress, a critical heat flux separates cases with growing and decaying phytoplankton populations. Using the LES results, we characterize the critical windstress and critical heat flux in terms of other physical and biological parameters and propose a simple expression for each based on the analysis of the analytical model. Phytoplankton growth begins when the mixing depth shoals above the critical depth, consistent with the critical depth hypothesis. Our results provide a framework to interpret blooms in other conditions where both the depth and the intensity of turbulent mixing might be crucial factors in influencing phytoplankton growth.

Keywords: critical depth, critical turbulence, large-eddy simulation, mixing depth, phytoplankton bloom, turbulent diffusivity.

Introduction

The striking scene of phytoplankton amassing in the surface boundary layer during spring—the spring bloom—has fascinated scientists for decades. Early work by Gran and Braarud (1935) and Riley (1946) suggested that the spring bloom begins when the mixed layer depth first shoals above a critical depth. About 60 years ago, Sverdrup (1953) formalized the "critical depth hypothesis" and derived an expression for the critical mixed layer depth based on several assumptions. Among these, he assumed that: phytoplankton cells are uniformly distributed in the mixed layer; phytoplankton growth at the onset of the bloom is not limited by nutrient availability; the depth-dependent cellular growth rate is proportional to the available light which decreases exponentially with depth from a surface maximum; and the combined loss rate, which incorporates all sources of phytoplankton loss, including mortality due to grazing, and losses due to sinking, viral infection, and parasitism, is independent of depth.

Prompted by observations of phytoplankton blooms preceding mixed layer shoaling (Townsend *et al*., 1994; Behrenfeld, 2010; Boss and Behrenfeld, 2010), several recent studies have proposed refinements or alternatives to the critical depth hypothesis involving physical and/or biological triggers of the spring bloom (Huisman *et al*., 1999; Behrenfeld, 2010; Chiswell, 2011; Taylor and Ferrari, 2011a, b; Mahadevan *et al*., 2012). Here, we will consider only physical mechanisms, specifically wind-driven turbulence and the development of stratification through net surface heating. We do not attempt to rule out biological drivers of the spring bloom, such as the dilution-recoupling hypothesis proposed by Behrenfeld (2010). Our goal is not to reproduce a given spring bloom event, but instead to examine the possible role of physical drivers on phytoplankton growth during the spring bloom.

Although Sverdrup (1953) used the mixed layer depth, defined using measured temperature and salinity profiles, as a proxy for the depth of active mixing, these depths are not always equal (Brainerd and Gregg, 1995). The mixed layer depth is often defined in terms of a fixed density or temperature difference from the surface and reflects the maximum depth of past mixing, whereas the "mixing depth" is the depth to which currently active turbulence penetrates. When the mixing depth is shallower than the mixed layer depth, the former is a more appropriate choice for comparison with the critical depth (Brody and Lozier, 2014).

Huisman *et al.* (1999) considered a scenario where the rate of mixing is not sufficient to maintain a uniform phytoplankton concentration in the mixing layer. Using a one-dimensional column model with the rate of change of phytoplankton concentration balanced by growth, losses, and diffusion, they showed that a bloom could be triggered either by a reduction in the mixing depth or by a reduction in the strength of mixing within this layer. When the mixing depth is significantly deeper than the critical depth, blooms occur in their model when the turbulent diffusivity, κ_T, is less than a critical value, κ_c, the so-called "critical turbulence hypothesis". This scenario was anticipated by Sverdrup (1953) who stated: "a phytoplankton population may increase independently of the thickness of the mixed layer if the turbulence is moderate".

The "critical turbulence" hypothesis can also be interpreted in terms of characteristic time-scales (Taylor and Ferrari, 2011b). Mixing occurs on a time-scale that depends on the size and intensity of the turbulent motions responsible for stirring phytoplankton cells down from the ocean surface. On the other hand, phytoplankton cells accumulate in regions where local growth outweighs losses with a characteristic growth time-scale. When the mixing time-scale is very fast relative to the growth time-scale, the phytoplankton concentration is expected to remain relatively uniform, in agreement with Sverdrup's assumption. On the other hand, when mixing is slow compared with the growth time-scale, this assumption may no longer be valid, and a bloom can occur through the critical turbulence mechanism.

Taylor and Ferrari (2011b) applied the critical turbulence hypothesis to study phytoplankton blooms following a period of thermal convection. In the absence of lateral processes, such as eddy-induced slumping (Taylor and Ferrari, 2011a; Mahadevan *et al.*, 2012), they asserted that the spring bloom could be triggered by a shutdown of thermal convection. This hypothesis was supported by Ferrari *et al.* (2014) using satellite observations of near-surface Chlorophyll concentration and heat flux from an atmospheric reanalysis dataset from the North Atlantic. Taylor and Ferrari (2011b) assumed that in winter, turbulence in the mixed layer is driven primarily by thermal convection, whereas winds play a secondary role.

After the shutdown of thermal convection, phytoplankton growth could still be suppressed as long as wind-driven mixing is sufficiently strong. Chiswell (2011) suggested that strong winds could delay the spring bloom, with a bloom occurring only after the windstress drops below a critical threshold. Since density stratification generally suppresses turbulence, the level of windforcing needed to suppress a bloom is expected to increase with increasing net surface heating. This suggestion was supported by Brody *et al.* (2013) who found that a stabilizing heat flux was not always sufficient to trigger a bloom. An important open question remains: what is the value of the critical windstress and how does it change in response to a stabilizing surface heat flux?

Here, we will seek to identify how the critical windstress depends on important parameters including the stabilizing surface heat flux and the critical depth. We will address this question using large-eddy simulations (LES) that resolve the largest turbulent overturns in a wind-driven Ekman layer. By systematically varying the surface windstress and the stabilizing heat flux across a suite of simulations, we will examine when phytoplankton blooms develop. We will then use the results from the LES to develop an analytical model, extending previous work by Huisman *et al.* (1999), Ebert *et al.* (2001), and Taylor and Ferrari (2011b) to explicitly include the effects of wind-forcing and surface heating. The analytical model could help predict how a given seasonal progression of surface wind and heat fluxes might lead to the onset of the spring bloom and provides a framework to interpret blooms in observations and models with more complicated biogeochemistry.

This paper is divided into the following main sections: a description of the setup and results of the LES and an overview of the development of an analytical model in a heated, wind-driven Ekman layer. After discussion and conclusions, an appendix contains a comparison of LES and analytical phytoplankton model results.

Large-eddy simulations

Setup

To study the influence of wind-driven mixing and surface heating on phytoplankton growth, we use high-resolution, three-dimensional LES of the wind-forced turbulent Ekman layer, as illustrated in Figure 1. In each simulation, turbulence is generated by imposing a constant surface windstress, τ_{wind}. Some simulations also include a constant, positive net surface heat flux, Q_0. Note that since we do not explicitly include a diurnal cycle in our model, Q_0 is intended to represent the time-averaged net surface heat flux. Taylor and Ferrari (2011b) simulated the mixing due to a typical diurnal cycle using LES and found that it was insufficient to prevent a phytoplankton bloom. The complete list of simulation parameters is listed in Table 1. Our parameter space for Q_0 ranges from 0 to 75 W m^{-2} whereas our parameter space for τ_{wind} ranges from 0.01 to 0.2 Pa. Although we focus on the coupling effects of surface heating and winds, our parameter space covers typical spring values.

LES explicitly resolve the largest, most energetic three-dimensional turbulent motions and model the influence of smaller scales. In this methodology, a spatial filter, denoted here by an overbar, $^{-}$, is applied to the governing equations. The LES then time-steps the following filtered equations for the three components of velocity, $\bar{\mathbf{u}}$, buoyancy, $\bar{b}$, phytoplankton cell concentration, $\bar{P}$, and the continuity equation:

$$\frac{\partial \bar{\mathbf{u}}}{\partial t} + \bar{\mathbf{u}} \cdot \nabla \bar{\mathbf{u}} + f\hat{\mathbf{k}} \times \bar{\mathbf{u}} = -\frac{1}{\rho_0}\nabla \bar{p} + \bar{b}\hat{\mathbf{k}} - \nabla \cdot \tau^{\text{SGS}} + \nu \nabla^2 \bar{\mathbf{u}}, \quad (1)$$

$$\frac{\partial \bar{b}}{\partial t} + \bar{\mathbf{u}} \cdot \nabla \bar{b} = -\nabla \cdot \lambda_{\text{b}}^{\text{SGS}} + \kappa_{\text{b}} \nabla^2 \bar{b}, \quad (2)$$

$$\frac{\partial \bar{P}}{\partial t} + \bar{\mathbf{u}} \cdot \nabla \bar{P} = (\mu(z) - m)\bar{P} - \nabla \cdot \lambda_{\text{P}}^{\text{SGS}} + \kappa_{\text{P}} \nabla^2 \bar{P}, \quad (3)$$

$$\nabla \cdot \bar{\mathbf{u}} = 0. \quad (4)$$

The left hand sides of Equations (1)–(3) include advection by the resolved three-dimensional velocity field. Unresolved subgrid-scale (SGS) processes are represented through $\boldsymbol{\tau}^{\mathrm{SGS}}$, $\boldsymbol{\lambda}_{\mathrm{b}}^{\mathrm{SGS}}$, and $\boldsymbol{\lambda}_{\mathrm{P}}^{\mathrm{SGS}}$, which denote the SGS stress, buoyancy flux, and phytoplankton flux, respectively. The form of the SGS contributions is described below. The molecular viscosity, ν, is set to $10^{-6}\ \mathrm{m^2\,s^{-1}}$. The Prandtl numbers of phytoplankton and buoyancy, $\mathrm{Pr_P}$ and $\mathrm{Pr_b}$, are equal to 1 and 7 (Taylor and Ferrari, 2010), respectively, such that $\kappa_{\mathrm{P}} = \nu$ and $\kappa_{\mathrm{b}} = \nu/7$. However, since the molecular transport is negligible in all simulations, our results are insensitive to the value of these parameters. We apply the Boussinesq approximation and symbolize the background density as ρ_0.

Since our focus is on the influence of turbulent mixing on phytoplankton growth, we use a highly simplified phytoplankton model in Equation (3). In particular, we follow Sverdrup (1953) and Taylor and Ferrari (2011a, b) in assuming that the local growth rate, $\mu(z)$, is a prescribed function of depth only and that the loss rate, $m = 0.1\ \mathrm{d^{-1}}$, is constant in space and time. The prescribed local growth rate is $\mu(z) = \mu_0 \mathrm{e}^{-z/h_{\mathrm{L}}}$ where $\mu_0 = 1\ \mathrm{d^{-1}}$ is the maximum growth rate at the ocean surface, and $h_{\mathrm{L}} = \{5\ \mathrm{m}, 10\ \mathrm{m}\}$ is the *e*-folding depth associated with light penetration. The values of the biological parameters used in this study, μ_0, m, and h_L, can be found in Tables 1 and 2. The growth rate is a function of the average light availability from the past day. Phytoplankton cells are allowed to move vertically and they instantly adapt to the light availability at each depth. The instantaneous growth rate is a function of depth alone and so we neglect phytoadaptation (Cullen and Lewis, 1988) or growth rate dependence on past history. Both effects can be included if a particle-based Lagrangian approach is taken instead of an Eulerian model (Broekhuizen, 1999; Nagai *et al.*, 2004; Ross and Sharples, 2004; Yamazaki *et al.*, 2014). For simplicity, the local growth and loss rates, μ_0 and m, are assumed to be constant in time. As a result, we do not consider interactions between phytoplankton, nutrients, and zooplankton, which would modulate the growth and loss rates. We also neglect other processes including cell sinking/buoyancy and motility, since phytoplankton cell capacities are too weak to counteract the mixing intensity. Despite these simplifications, the response of the three-dimensional phytoplankton concentration to resolved and SGS turbulence is non-trivial.

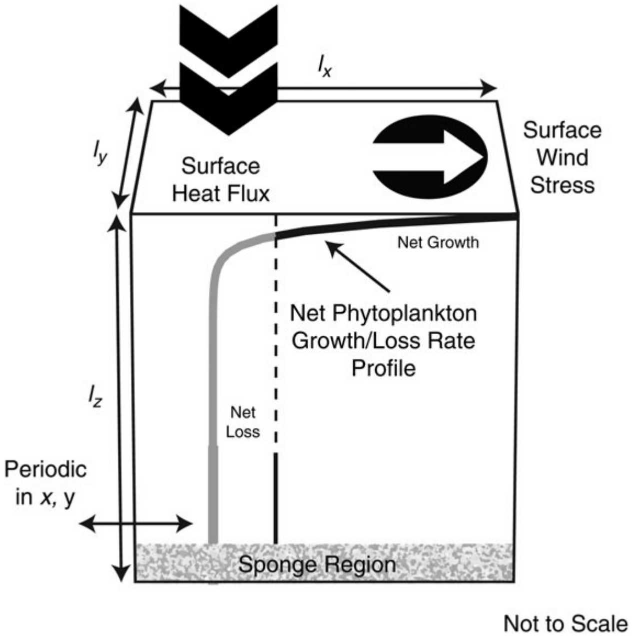

Figure 1. Schematic of the LES domain. The domain lengths, l_x, l_y, and l_z, are listed in Table 1. The lateral boundary conditions are periodic and the bottom boundary includes a sponge region. For each simulation, a constant surface windstress and/or a surface heat flux is applied. The growth model assumes that phytoplankton cell concentration growth is light-limited and that the biological parameters are constant in time.

The values for the biological parameters, μ_0, m, and h_{L} (Table 2), are selected for comparison with simulations that examine the beginning of phytoplankton blooms with steady convection, without a surface windstress, and a critical depth of 50 m (Taylor and Ferrari, 2011b). We include an additional value of $h_{\mathrm{L}} = 10$ m to study if and how the critical wind changes for a critical depth of 100 m.

Details of the numerical method are given in Taylor (2008) and we use the same method as Taylor and Ferrari (2011b), except that we use a different model for the SGS terms. The stable wind-driven boundary layer, typical in spring and summer, is much shallower than the convective boundary layer found in winter. The depth of the stable wind-driven boundary is subject to the strengths of the surface wind and the surface heating. Although wind deepens the boundary layer by approximately the Ekman depth, the surface heating provides stability and shallows the boundary layer. Previously, Mason and Derbyshire (1990) demonstrated that the constant Smagorinsky model, used in Taylor and Ferrari (2011b), might not be appropriate for simulating stable boundary layers where stratification can suppress turbulent production. This led to the development of SGS models suitable for the stable boundary layer (e.g. Kosović and Curry, 2000; Basu and Porté-Agel, 2006; Beare *et al.*, 2006; Zhou and Chow, 2011; Enriquez, 2013). Here, we use the dynamic Wong–Lilly model, which has been previously applied to study the stable atmospheric boundary layer (Zhou and Chow, 2011, 2012), where the dynamics are analogous to the stable wind-driven boundary layer considered here (Lien and

Table 1. Parameters for LES.

l_x, l_y, l_z (m)	n_x, n_y, n_z	h_{L} (m)	h_{c} (m)	τ_{wind} (Pa)	Q_0(W m^{-2})
100, 100, 150	128, 128, 120	5	50	0.001*, 0.01	0
100, 100, 150	64, 64, 120	5	50	0.02, 0.04, 0.06	0
100, 100, 150	64, 64, 120	5	50	0.08, 0.10	0, 5, 25, 50, 75
150, 150, 225	64, 64, 120	10	100	0.10, 0.15, 0.20	0, 5, 25, 50, 75

The simulations use a domain size of l_x, l_y, l_z, using n_x, n_y, n_z computational grid-points. The simulations vary the light *e*-folding depth, h_{L}, the critical depth, h_c, the windstress, τ_{wind}, and the surface heat flux, Q_0. The first set of simulations includes unheated cases forced with a surface windstress. The LES with $\tau_{\mathrm{wind}} = 0.001$ Pa is an extremely low windstress case that is only used in Figure A3. The second set of simulations includes cases forced with surface heating and windstress.

Table 2. Chosen physical, biological, and numerical parameters for LES.

	Symbol	Value
Physical parameter		
Coriolis parameter	f	10^{-4} s^{-1}
Background density	ρ_0	1000 kg m^{-3}
Specific heat capacity	c_p	4×10^3 J kg^{-1}°C^{-1}
Thermal expansion coefficient	α	1.65×10^{-4}°C^{-1}
Gravitational acceleration	g	9.81 m s^{-2}
Biological parameter		
Maximum specific growth rate	μ_0	1 d^{-1}
Specific loss rate	m	0.1 d^{-1}
e-folding depth associated with light penetration	h_L	5, 10 m
Numerical parameter		
Molecular viscosity	ν	10^{-6} m^2 s^{-1}
Molecular diffusivity	κ	10^{-6} m^2 s^{-1}
Buoyancy Prandtl number	$\mathrm{Pr_b}$	7
Phytoplankton Prandtl number	$\mathrm{Pr_P}$	1

Sanford, 2004). The SGS stress tensor is modelled as:

$$\boldsymbol{\tau}^{\mathrm{SGS}} = -2\nu_{\mathrm{SGS}}\bar{\mathbf{S}}, \tag{5}$$

where $\bar{\mathbf{S}} = (\nabla\bar{\mathbf{u}} + \nabla\bar{\mathbf{u}}^T)/2$ is the rate of strain tensor. The dynamic eddy viscosity, ν_{SGS}, is given by $\nu_{\mathrm{SGS}} = C_\varepsilon\Delta_f^{4/3}$. The local horizontal test filter width, Δ_f, is equal to twice the grid spacing, Δ_g. The dynamic coefficient C_ϵ is determined using the least-squares method of Lilly (1992), which results in an eddy viscosity that varies in space and time. The SGS buoyancy and phytoplankton flux terms in Equations (2) and (3) are modelled as:

$$\boldsymbol{\lambda}_{\mathrm{b}}^{\mathrm{SGS}} = -\kappa_{\mathrm{SGS}}\nabla\bar{b}, \tag{6}$$

$$\boldsymbol{\lambda}_{\mathrm{P}}^{\mathrm{SGS}} = -\kappa_{\mathrm{SGS}}\nabla\bar{P}, \tag{7}$$

where κ_{SGS} is the SGS diffusivity. We set the SGS Prandtl numbers of phytoplankton and buoyancy, equal to 1 such that $\kappa_{\mathrm{SGS}} = \nu_{\mathrm{SGS}}$.

Windforcing is represented by applying a constant stress boundary condition at the top of the domain. Here, the x-axis is aligned with the windstress, and (u,v,w) will denote the velocity in the downwind, cross-wind, and vertical directions, respectively. Surface heating is represented by applying a uniform buoyancy flux as a boundary condition to Equation (2). Since the smallest mixing depth in our simulations is ~25 m, the added buoyancy is quickly mixed down from the surface. To limit the number of parameters in this study, we do not include penetrative heating. However, it would be interesting to include this process in future work. Although the LES model solves for buoyancy, if we assume a linear equation of state and neglect freshwater inputs at the surface, the surface buoyancy flux, B_0, can be related to an equivalent surface heat flux, Q_0:

$$B_0 = \frac{Q_0\alpha g}{c_p\rho_0}, \tag{8}$$

where α is the thermal expansion coefficient, g the gravitational acceleration, c_p the specific heat capacity, and ρ_0 a background density (see Table 2 for values).

We use a computational domain size of $l_x = 100$, $l_y = 100$, and $l_z = 150$ m for simulations with $h_\mathrm{L} = 5$ m, and a domain of $l_x = 150$, $l_y = 150$, and $l_z = 225$ m for simulations with $h_\mathrm{L} = 10$ m. For both domains, we use $n_x = 64$, $n_y = 100$, and $n_z = 120$ m gridpoints. The resolution of the simulation with a windstress, τ_{wind}, equal to 0.01 Pa and $Q_0 = 0$ W m^{-2}, is higher to ensure that we resolve the largest turbulent motions in the thinner Ekman layer. The domain size is comparable with previous simulations of an unstratified wind-driven Ekman layer (Zikanov *et al.*, 2003). The grid is stretched in the vertical direction to resolve small-scale turbulence near the surface. For the smaller domain, the minimum and maximum vertical grid spacings are 0.3 and 2.3 m, respectively. For the larger domain, the minimum and maximum vertical grid spacings are 0.4 and 3.5 m, respectively. Following Taylor and Ferrari (2011b), we use boundary conditions that approximate an unbounded domain without large-scale horizontal gradients. Specifically, periodic boundary conditions are applied in the horizontal directions. A sponge region is placed in the lower 15% of the domain to prevent interactions between the flow and the lower boundary.

For each case, there is a 12-h initialization period. At the start of this period, we prescribe a uniform buoyancy profile, and the velocity is initialized by applying random fluctuations with an amplitude of 0.001 m s^{-1} with no mean flow. During the first 9 h of the initialization period, the windstress and surface heat flux are increased linearly from zero to the value specified in Table 1. The windstress and surface heat flux remain at this value for the remaining 3 h of the initialization period and the remaining 8 d of each simulation. After the 12 h initialization period, we initialize the phytoplankton concentration with a uniform profile and reset the simulation time to $t = 0$ d. Mean values are calculated by averaging over horizontal planes and are denoted by $\langle\ \rangle$. Phytoplankton concentrations are normalized by the initial concentration, P_0, or the average surface concentration at a given time, $\langle P_{s,t}\rangle$.

Results

Before discussing the effects of surface windstress and heating flux on phytoplankton dynamics, we briefly describe the mean velocity and buoyancy fields. Figure 2a and b depicts the mean horizontal velocities, $\langle\bar{u}\rangle$ and $\langle\bar{v}\rangle$, for $\tau_{\mathrm{wind}} = 0.08$ Pa and $Q_0 = 0$, 25, 75 W m^{-2}, averaged from $t = 0$ to $t = 8$ d. Our simulations in the cases with $Q_0 = 0$ W m^{-2} have been validated by comparing with results from Zikanov *et al.* (2003), and our mean velocity profiles closely match their results. As the level of heating increases, the Ekman flow becomes confined to a shallower region and the maximum magnitude of the cross-wind component, $\langle\bar{v}\rangle$, increases. This is consistent with the confinement effects in a stable bottom Ekman layer reported in Taylor and Sarkar (2008).

Mean buoyancy profiles, $\langle\bar{b}\rangle$, are shown in Figure 2c. For the case in which $Q_0 = 0$, the buoyancy remains zero since there is no source of buoyancy. However, the addition of surface heating leads to a non-uniform buoyancy profile. The warm (buoyant) fluid is confined to a layer near the surface, and this layer is shallower with stronger heating. Note that the non-uniform profiles of buoyancy translate to relatively small changes in temperature. The mixed layer depth is often defined in terms of a fixed density or temperature difference from the surface. For example, a metric used to define the mixed layer depth is a temperature change of 0.8°C (Kara *et al.*, 2000). From Figure 2c, the buoyancy change from the surface for the $\tau_{\mathrm{wind}} = 0.08$ Pa, $Q_0 = 75$ W m^{-2} case is $\sim 5.0 \times 10^{-4}$ m s^{-2}, which corresponds to a temperature change of just 0.3°C, smaller

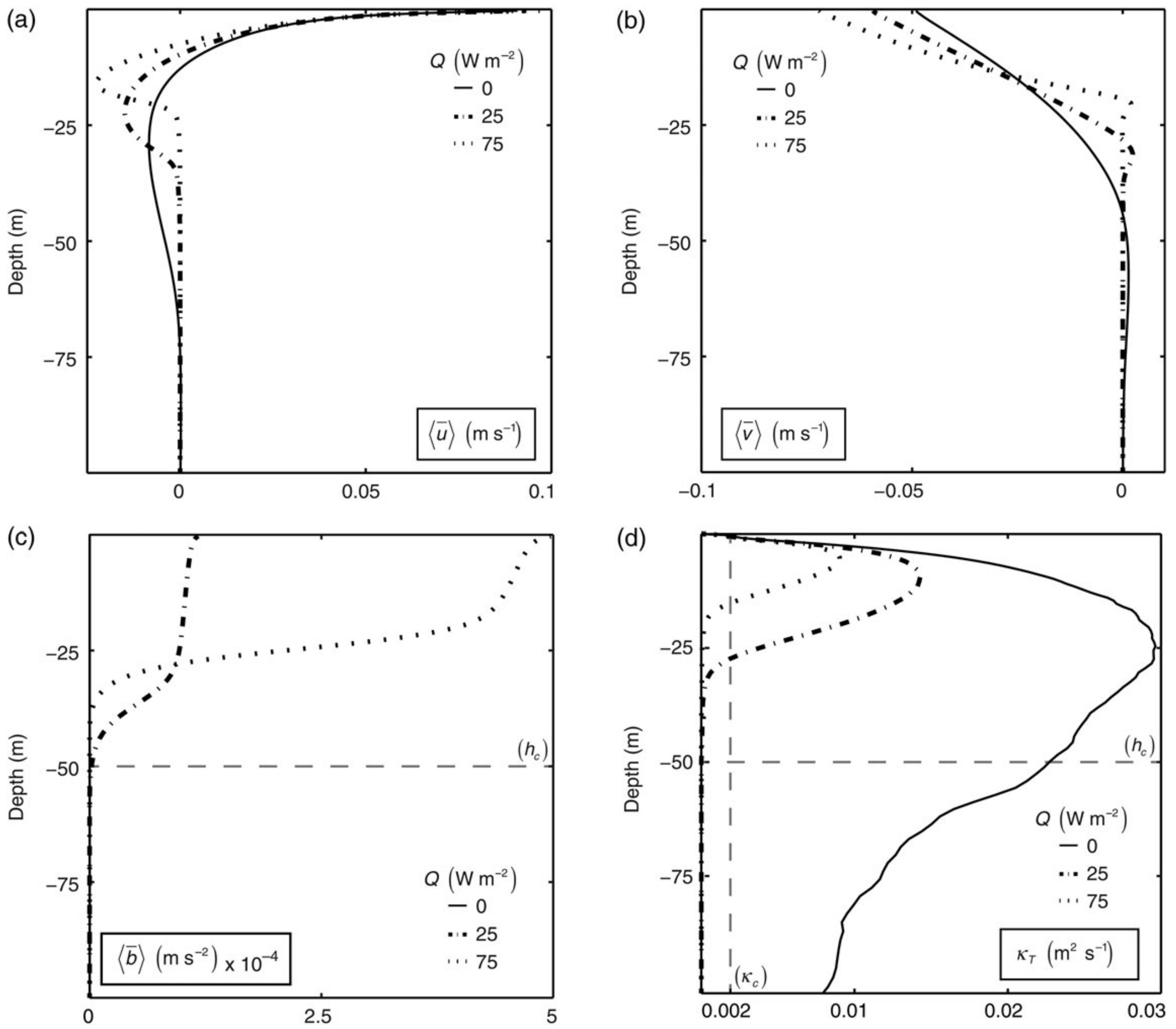

Figure 2. Profiles of the resolved mean velocities, (a) $\langle\bar{u}\rangle$ and (b) $\langle\bar{v}\rangle$, (c) buoyancy, $\langle\bar{b}\rangle$, and (d) total turbulent diffusivity, κ_T, from the LES with $\tau_{\text{wind}} = 0.08$ Pa and $Q_0 = 0$, 25, and 75 W m^{-2}. Profiles are averaged from $t = 0$ to $t = 8$ d. For these cases, the critical depth, h_c, is 50 m, and the critical diffusivity, κ_c, is 0.002 m^2 s^{-1}.

than the Kara *et al.* (2000) mixed layer depth criterion. Similarly, other methods to find the mixed layer depth (e.g. Holte and Talley, 2009) would also classify our full domain as the mixed layer.

Profiles of the turbulent diffusivity of phytoplankton, κ_T, shown in Figure 2d, highlight how a stabilizing surface heat flux limits the vertical extent of phytoplankton mixing. Here, the turbulent diffusivity is defined as the sum of the mean SGS diffusivity, $\langle\kappa_{\text{SGS}}\rangle$, and the resolved turbulent diffusivity diagnosed from the LES fields:

$$\kappa_T = \frac{\langle\kappa_{\text{SGS}}\rangle - \langle\bar{w}\bar{P}\rangle}{\partial\langle\bar{P}\rangle/\partial z}. \tag{9}$$

For all cases, the SGS diffusivity accounts for less than 10% of the total diffusivity. For the LES here, the largest SGS diffusivity contributions are located near the surface. Additionally, the SGS contribution increases with surface heating since the length scales become smaller. As the level of heating increases, the magnitude of κ_T decreases and the mixing depth shallows. Note that in the case with $Q_0 = 0$, mixing extends well below the critical depth, $h_c \equiv h_L\mu_0/m = 50$ m. Taylor and Ferrari (2011b) derived a useful approximate expression for the critical turbulent diffusivity:

$$\kappa_c \simeq \frac{h_L^2}{m}(\mu_0 - m)^2. \tag{10}$$

In all three cases shown in Figure 2d, the maximum turbulent diffusivity is larger than the critical turbulent diffusivity, $\kappa_c \simeq 0.002$ m^2 s^{-1}.

Figure 3 shows a three-dimensional snapshot of the phytoplankton concentration for the simulation with $\tau_{\text{wind}} = 0.08$ Pa and $Q_0 = 5$ W m^{-2}. In this case, the phytoplankton are largely confined to the warm layer near the surface, although three-dimensional fluctuations in the phytoplankton concentration are still clearly visible. The level of variability in the three-dimensional phytoplankton concentration at each depth can be quantified with the horizontal variance, shown in Figure 4. Here, the square root of the variance is

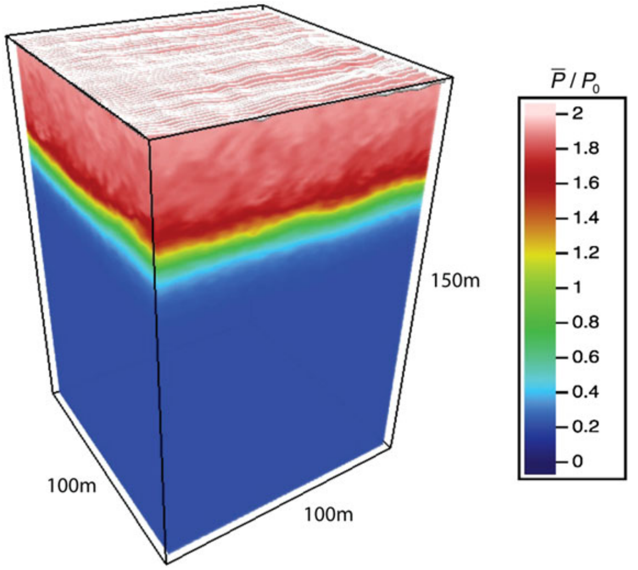

Figure 3. Resolved phytoplankton concentration from the LES simulation with $\tau_{\text{wind}} = 0.08$ Pa and $Q_0 = 5$ W m^{-2}. Phytoplankton concentrations are normalized by P_0, the initial phytoplankton concentration at $t = 0$ d. White lines show instantaneous streaklines at the sea surface. In this simulation, the phytoplankton concentration is highly confined to a relatively thin mixing layer, although fluctuations in the phytoplankton concentration are still visible within the mixing layer itself.

normalized by the local mean concentration to aid comparison between the cases. Without heating, fluctuations in the phytoplankton concentration are relatively small. The normalized variance in this case increases somewhat with depth, although this is partly a reflection of a decrease in the mean concentration with depth. With surface heating, the normalized phytoplankton variance is large at the base of the active mixing layer.

Figure 5 shows the evolution of the horizontally averaged phytoplankton concentration as a function of depth for the three simulations shown in Figure 2d. Profiles are at $t = 0, 2, 4, 6, 8$ d. For these cases, the critical depth, h_c, is 50 m, and the corresponding e-folding depth associated with light penetration, h_L, is 5 m. The suppression of turbulent mixing and the restriction of the mixing depth cause a regime change in the phytoplankton response. In the case with $Q_0 = 0$, the phytoplankton concentration decreases in time at all depths and the concentration is modestly surface-intensified. The lack of a bloom is consistent with strong mixing with $\kappa_T > \kappa_c$ over a layer deeper than the critical depth. In contrast, the cases with a positive surface heat flux exhibit phytoplankton growth.

In the positive surface heat flux cases shown in Figure 5, the mixing depths inferred from the vertical phytoplankton flux profiles are shallower than the critical depth, and the mixing depths clearly delineate regions of high and low phytoplankton concentration. The simulations with $h_c = 100$ and $h_L = 10$ m show comparable behaviour to the simulations with $h_c = 50$ and $h_L = 5$ m; If the windstress is above a critical threshold, phytoplankton cell concentration decays over time. Additional surface heating may suppress the turbulence and allow phytoplankton cell concentration to increase.

To quantify the mixing depth from the LES, we calculate the depth at which the vertical phytoplankton flux is less than 5% of the maximum vertical phytoplankton flux, $\langle w'P'\rangle/\langle w'P'\rangle_{\max} = 0.05$.

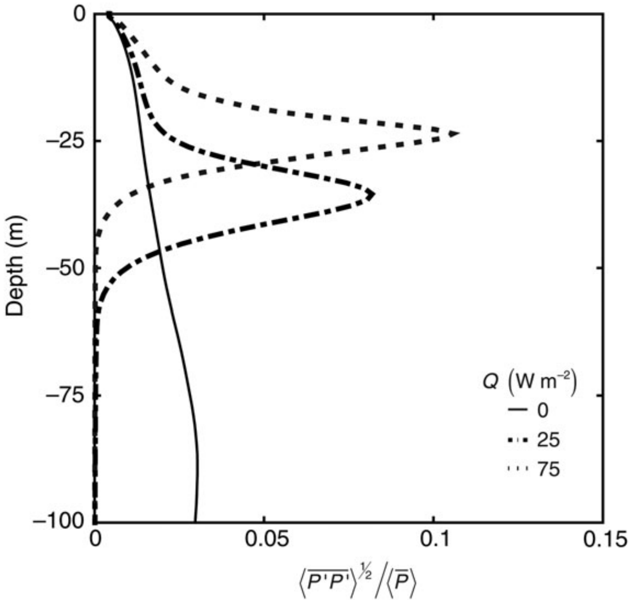

Figure 4. Profiles of the ratio of the square root of the averaged phytoplankton concentration variance to mean phytoplankton concentration, $\langle P'P'\rangle^{1/2}/\langle P\rangle$ from the LES with $\tau_{\text{wind}} = 0.08$ Pa and $Q_0 = 0$ W m^{-2}. Profiles are averaged from $t = 0$ to $t = 8$ d. For this case, the critical depth, h_c, is 50 m.

The mixing depth diagnosed from the LES using this threshold allows us to identify the influence of mixing depth on bloom initiation. Figure 6 displays the calculated mixing depths as a function of surface windstress and heat flux for $h_L = 5$, $h_c = 50$ m (a) and $h_L = 10$, $h_c = 100$ m (b). As the windstress increases the mixing depth increases. For a given windstress, the mixing depth decreases with additional surface heating. Filled symbols in Figure 6 indicate simulations with positive net phytoplankton growth. Net growth occurs where the mixing depth is shallower than the critical depth, consistent with the critical depth hypothesis if the mixing depth is used instead of the mixed layer depth.

The mixing depth diagnosed from the LES output can also be used to quantify the net phytoplankton growth rates. The evolution of the depth-averaged phytoplankton concentration from the LES for all cases with $h_L = 5$ m (corresponding to $h_c = 50$ m) is shown in Figure 7. Here, the phytoplankton concentration was averaged over horizontal planes and within the diagnosed mixing depth and normalized by the initial concentration:

$$P_{\text{avg},t} = -\frac{1}{L}\int_{-L}^{0} \frac{\langle \bar{P}\rangle}{P_0}\,\mathrm{d}z, \qquad (11)$$

where L is the mixing depth diagnosed from the LES using the method described above. For all cases shown with $Q_0 = 0$, the depth-averaged phytoplankton concentration decreases in time. On the other hand, sufficiently large surface heat fluxes can lead to net growth (Figure 7b).

The net phytoplankton growth rates from the LES can be calculated from the depth-averaged phytoplankton concentration:

$$\sigma = \ln \frac{P_{\text{avg},t_2}/P_{\text{avg},t_1}}{t_2 - t_1}. \qquad (12)$$

We calculate the exponential growth rates using $P_{\text{avg},t}$ at $t_1 = 4$ and $t_2 = 8$ d and plot them for all cases in Figure 8. Increasing the

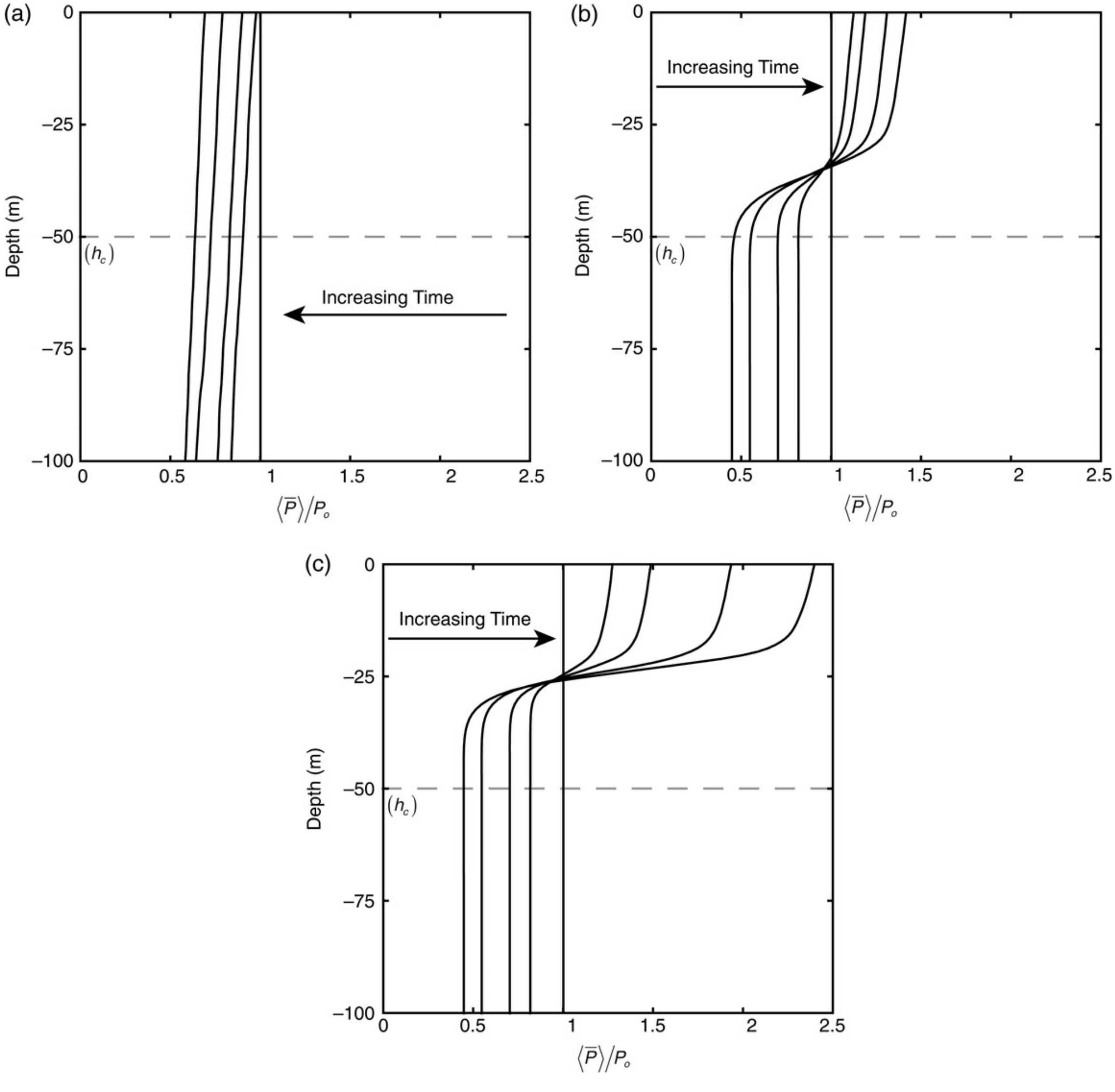

Figure 5. Profiles of the resolved mean phytoplankton cell concentration, $\langle \overline{P}\rangle/P_0$, at $t = 0, 2, 4, 6$, and 8 d from the LES with $\tau_{\text{wind}} = 0.08$ Pa and (a) $Q_0 = 0$ W m^{-2}, (b) $Q_0 = 25$ W m^{-2}, and (c) $Q_0 = 75$ W m^{-2}. Phytoplankton concentrations are normalized by P_0, the initial phytoplankton concentration at $t = 0$ d. The critical depth, h_c, is 50 m, and the corresponding e-folding depth associated with light penetration, h_L, is 5 m for these simulations.

surface windstress leads to slightly lower growth rates, whereas increasing the surface heat flux leads to higher growth rates. If the resulting growth rate is positive, it is classified as growth, and negative if otherwise. Additionally, Figure 6 shows that there is growth when the mixing depths are shallower than the critical depth and decay if the mixing depth is greater than the critical depth.

Analytical phytoplankton concentration model

Although the LES simulates the response of phytoplankton to wind-driven turbulence and surface heating, the computations are expensive, which limits our ability to explore the influence of various parameters. In this section, we will develop an analytical model for the phytoplankton concentration in a heated, wind-driven Ekman layer using a method similar to that described in Taylor and Ferrari (2011b). The analytical model will be used to derive approximate expressions for the critical windstress and critical surface heat flux in terms of other physical and biological parameters. In this section, we will first introduce the form of the analytical model, then describe parameterizations for the mixing depth and turbulent diffusivity for the wind-driven and surface-heated cases. Results of the new model are described in the "Results from the analytical model" section.

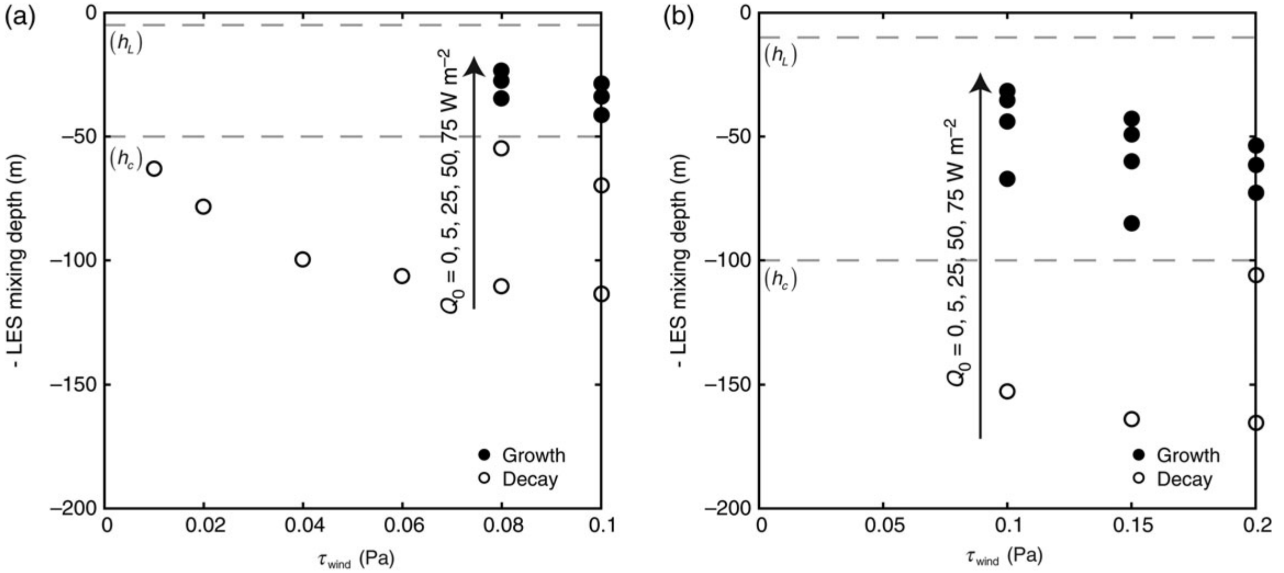

Figure 6. LES mixing depths as a function of the surface windstress for (a) $h_c = 50$ m ($h_L = 5$ m) and (b) $h_c = 100$ m ($h_L = 10$ m). The surface heat flux varied from 0 to 75 W m^{-2}. For a given windstress, increasing the surface heat flux leads to shallower mixing depths. The light *e*-folding depth, h_L, and the critical depth, h_c, are indicated with grey dashed lines. Filled circles symbolize an LES exhibits phytoplankton growth and empty circles symbolize an LES exhibits phytoplankton decay.

Following Taylor and Ferrari (2011b), we begin by averaging the three-dimensional phytoplankton concentration equation [Equation (3)] across horizontal planes to obtain:

$$\frac{\partial}{\partial t}P(z,t) = (\mu(z) - m)P(z,t) + \tilde{\kappa}_T \frac{d^2}{dz^2}P(z,t), \qquad (13)$$

where $P(z,t)$ is the horizontally averaged phytoplankton concentration, and $\tilde{\kappa}_T$ represents mixing by resolved and SGS turbulence. Here, a uniform turbulent diffusivity profile is used and is symbolised by $\tilde{\kappa}_T$ to distinguish it from the turbulent diffusivity diagnosed from the LES, κ_T. Next, we seek exponentially growing/decaying solutions of the form $P(z,t) = \hat{P}(z)e^{\sigma t}$, in which σ is the net phytoplankton growth rate. Using this ansatz results in the following eigenvalue problem:

$$\sigma P(z,t) = (\mu(z) - m)\hat{P}(z) + \tilde{\kappa}_T \frac{d^2}{dz^2}\hat{P}(z). \qquad (14)$$

Solving Equation (14) yields a set of eigenvalues, σ_n, and corresponding eigenvectors, $\hat{P}_n$. The evolution of an arbitrary initial profile can then be expressed as a linear combination of the eigenvectors:

$$P(z,t) = \sum_n A_n^0 e^{\sigma_n t}\hat{P}_n(z), \qquad (15)$$

with the coefficients, A_n^0, chosen to match the initial conditions.

For a given set of parameters, we can compute the corresponding eigenvalues and eigenvectors with a uniform turbulent diffusivity profile within the mixing depth, L, and with no phytoplankton flux boundary conditions at $z = 0$ and $z = -L$. Under bloom conditions, when the phytoplankton population grows exponentially, we expect the most rapidly growing mode to dominate so that the growth rate eventually asymptotes to the largest eigenvalue, $\sigma \rightarrow \max(\sigma_n)$, regardless of the initial condition. If the largest growth rate is positive, $\max(\sigma_n) > 0$, a bloom may develop under the specified conditions. However, before we can interpret the dependence of the results on surface forcing, we need to develop formulations for the mixing depth, L, and the turbulent diffusivity, $\tilde{\kappa}_T$, as functions of the surface windstress and the heat flux.

Mixing depth and turbulent diffusivity scales

To express the mixing depth in terms of the surface forcing, we adapt the following form from Zilitinkevich and Baklanov (2002), which includes the effects of surface stress and a stabilizing surface buoyancy flux:

$$\frac{1}{L^2} = \frac{f^2}{(C_1 u_*)^2} + \frac{f B_0}{(C_2 u_*^2)^2}, \quad \text{for } B_0 \geq 0. \qquad (16)$$

Where C_1 and C_2 are prescribed constants, f the Coriolis parameter, $u_* \equiv (\tau_{\rm wind}/\rho_o)^{1/2}$ the friction velocity, and B_0 the surface buoyancy flux. Note that an increase in windstress will result in an increase in u^* and hence an increase in the mixing depth, L. Conversely, as the magnitude of the surface heat and buoyancy flux increase, the mixing depth will shallow.

The formulation in Equation (16) effectively interpolates between the turbulent Ekman depth, $\delta_{\rm Ekman} = u^*/f$, seen in the first term on the right hand side of Equation (16), and the depth of a stable boundary layer affected by a surface buoyancy flux and rotation, $\delta_{\rm SBL} = u_*^2/(fB_0)^{1/2}$ (Zilitinkevich, 1972), represented through the second term on the right hand side of Equation (16). Brody and Lozier (2014) specify separate and discontinuous mixing depths for small heat fluxes and large heat fluxes, whereas Equation (16) provides a continuous formulation for the mixing depth that is applicable from neutral to strongly stable regimes.

Recall from Figure 2d that the turbulent diffusivity and mixing depth both depend on the surface forcing. This distinguishes the

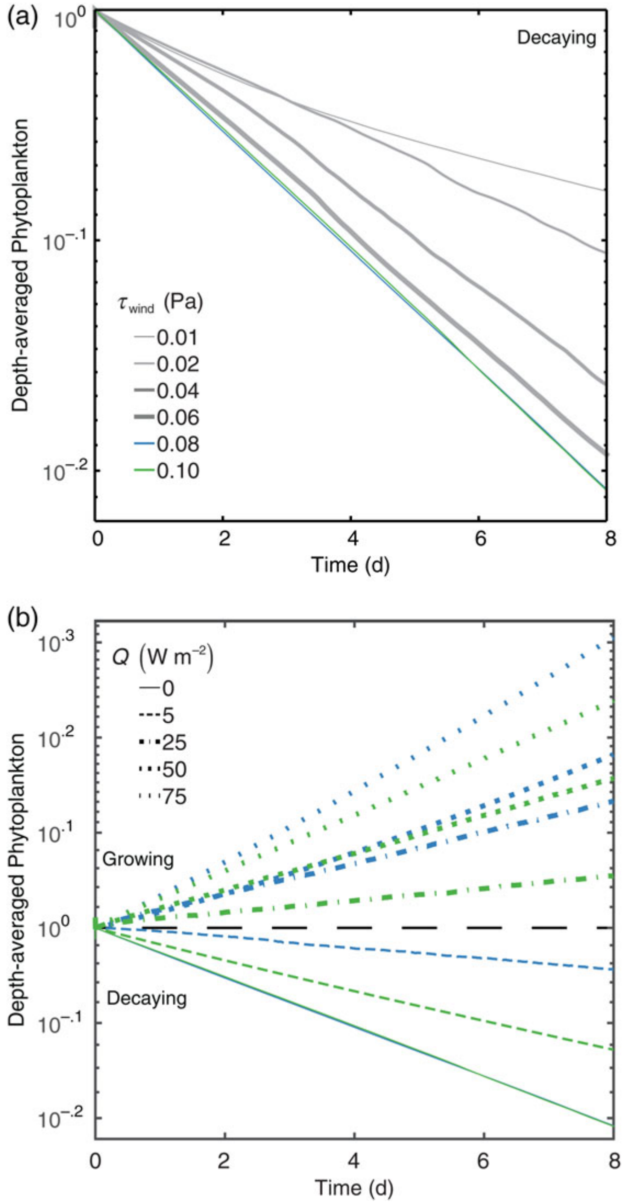

Figure 7. The evolution of the LES depth-averaged phytoplankton cell concentration within the mixing depth, *L*, normalized by the initial concentration, P_0. Cases at various (a) surface windstresses, τ_{wind}, with $Q_0 = 0$ and (b) surface heat fluxes, Q_0, are shown with the varying τ_{wind} shown in (a). Linestyles differentiate the values of Q_0 whereas colours distinguish the values of τ_{wind}. The plots shown are for the cases with $h_c = 50$ m (corresponding to $h_L = 5$ m).

dynamics of a heated, wind-forced boundary layer from scenarios considered in previous studies. For example, in considering thermal convection, Taylor and Ferrari (2011b) found that turbulence extends throughout the existing mixed layer, and varying the magnitude of the surface cooling influenced the intensity but not the depth of mixing. Here, we seek to develop a formulation for the turbulent diffusivity that captures the inter-dependence of the mixing depth and mixing intensity for the heated, wind-forced boundary layer.

To formulate a scaling for the turbulent diffusivity, $\tilde{\kappa}_T$, we use standard mixing length theory (e.g. Wyngaard, 2010). First, we define the eddy turnover time, $\tau = d/v$, using a characteristic turbulent length scale, d, and velocity scale, v. We assume that turbulence is generated by the surface windstress, in which case the friction velocity, $u^\star$, provides a characteristic turbulent velocity scale. We further assume that the largest turbulent motions dominate mixing and that their size scales with the mixing depth such that $d = L$ and $\tau = L/u^\star$. On dimensional grounds, the turbulent diffusivity will then scale with $\tilde{\kappa}_T \sim L^2/\tau$, or

$$\tilde{\kappa}_T = C_3 u_* L. \qquad (17)$$

Three coefficients, C_1, C_2, and C_3, are then needed to relate the mixing depth and turbulent diffusivity to the surface forcing. To determine the values of these coefficients, we use turbulent diffusivity profiles diagnosed from the LES. The coefficients are selected to produce a uniform $\tilde{\kappa}_T$ that best represents κ_T for a range of τ_{wind} and Q_0. Specifically, C_1 and C_2 are first chosen to produce the best collapse of the κ_T profiles. Then, C_3 is chosen so that the uniform $\tilde{\kappa}_T$ is representative of a depth-averaged κ_T.

Figure 9 shows the profiles of the normalized turbulent diffusivity, $\kappa_T^* = \kappa_T/(u_* L)$, plotted against the normalized depth, z/L, for the wind-only cases (Figure 9a) and the cases with surface heating (Figure 9b). In this figure, the approximate corresponding windspeed at 10 m above the sea surface for each windstress value is given for reference. Values are approximated with $\tau_{\text{wind}} = \rho_{\text{air}} C_D U_{10}^2$, where $\rho_{\text{air}} = 1.3$ kg m^{-3} is air density, and $C_D = 0.0013$ is the drag coefficient. These figures represent our choice of the pair of C_1 and C_2 that best collapse the κ_T^* profiles for all the cases, using the suggested range of $C_2 = 0.51 \pm 0.06$ (Zilitinkevich *et al.*, 2007). Setting $C_1 = 1$ and $C_2 = 0.57$ minimizes the error between all the κ_T^* profiles. We choose not to set C_1 based solely on the mixing depth of the wind-only simulations since there is a large spread in the resulting value of C_1. If the mixing depths of the wind-only simulations are used, the average value of C_1 is 1.45 with a standard deviation of 0.29. As seen in Figure 9b, the turbulent diffusivity profiles collapse well when normalized by $u^\star$ and L for all cases with $Q_0 \neq 0$. After selecting C_1 and C_2, we average the κ_T profiles from $z = 0$ to $z = -L$ and arrive at $C_3 = 0.02$, which is shown as vertical lines in Figure 9. Values of the analytical model coefficients used in this study are summarized in Table 3. Using a uniform diffusivity profile may affect the mean growth rates. The growth rates from the analytical solution are compared with LES results in the Appendix.

Comparing the normalized turbulent diffusivity profiles in Figure 9a and b, it is worth noting that the turbulent diffusivity extends deeper in the cases with $Q_0 = 0$ than in the cases with surface heating. We are unable to identify a set of coefficients C_1, C_2, and C_3 that produce the same mixing depth in the heated and unheated cases. We believe that this discrepancy is due to the development of a stable stratification at the base of the mixing layer in the heated cases, as seen in Figure 2c. This stable stratification inhibits mixing and somewhat reduces the mixing depth in cases with $Q_0 > 0$. It would be possible to explicitly include the effects of stratification (e.g. Zilitinkevich and Baklanov, 2002), but this would require solving an additional prognostic equation for the buoyancy. In an effort to keep the analytical model as simple as possible, our formulation depends only on the surface forcing. As will be shown in the next section, the analytical model produces an excellent agreement with the LES when $Q_0 > 0$, although when $Q_0 = 0$, the analytical model underestimates the mixing depth and consequently, overestimates the phytoplankton growth rate.

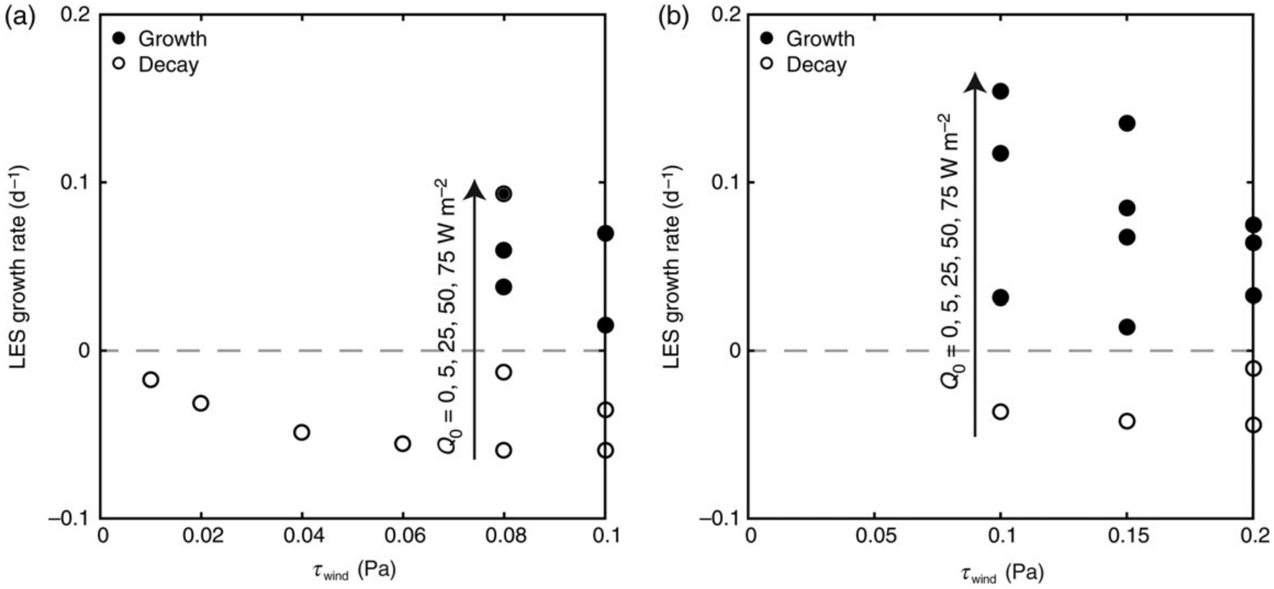

Figure 8. LES growth rates as a function of the surface windstress for (a) $h_c = 50$ m ($h_L = 5$ m) and (b) $h_c = 100$ m ($h_L = 10$ m). The surface heat flux varied from 0 to 75 W m^{-2}. For a given windstress, increasing the surface heat flux leads to higher growth rates. The grey dashed lines indicate zero growth. Filled circles symbolize an LES exhibits phytoplankton growth and empty circles symbolize an LES exhibits phytoplankton decay.

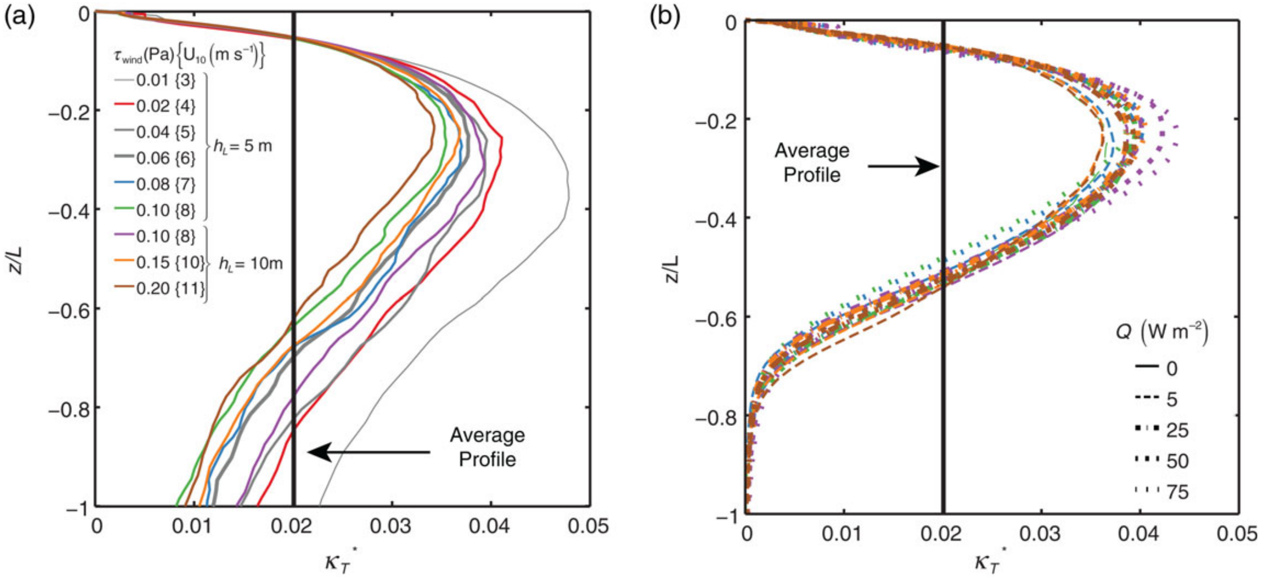

Figure 9. Normalized turbulent diffusivity profiles, $\kappa_T^* = \kappa_T/(u * L)$, diagnosed from the LES for various windstress, τ_{wind}, and surface heat flux, Q_0. Panel (a) shows cases with $Q_0 = 0$, and panel (b) shows profiles for various positive surface heat fluxes. Vertical lines indicate the average turbulent diffusivity from all the LES, which is used to acquire the coefficient C_3 for a uniform phytoplankton diffusivity model Equation (17). The corresponding wind at 10 m above the sea surface, U_{10}, is written next to the windstress values. Values are approximated with $\tau_{wind} = \rho_{air} C_D U_{10}^2$, where $\rho_{air} = 1.3$ kgm^{-3} is air density, and $C_D = 0.0013$ is the drag coefficient.

Results from the analytical model

In this section, we describe the predictions of the analytical model and compare the results with the LES and the critical depth and critical hypotheses. We solve Equation (14) using the formulation for the mixing depth and turbulent diffusivity described in the previous section. For comparison, we will start with the same biological

Table 3. Non-dimensional parameters for the mixing depth and vertical phytoplankton diffusivity model.

Parameter	Value
C_1	1.0
C_2	0.57
C_3	0.02

parameters as the LES, although the analytical model allows us to explore a much wider range of physical forcing and to derive expressions for the critical heat flux and critical windstress. Details of the parameter space used for the analytical model are in Table 4. In the first part of this section, we apply the same biological parameter values as in the LES, but use a wider range of surface windstress and heat flux. The sensitivity analysis that follows varies the biological parameters μ_0 and h_L, in addition to the wider range of surface windstress and heat flux.

Table 4. Parameters for the analytical model that complement the LES.

Δ_z (m)	μ_0 (d^{-1})	h_L (m)	Chl (mg m^{-3})	h_c (m)	τ_{wind} (Pa)	Q_0 (W m^{-2})
0.1	1	5	4	50	0.001 – 0.1	0 – 100
0.1	1	10	0.2	100	0.001 – 0.4	0 – 100
0.1	0.5	5	4	25	0.001 – 0.1	0 – 100
0.1	0.5	10	0.2	50	0.001 – 0.4	0 – 100
0.1	0.5	15	0.05	75	0.001 – 1.0	0 – 100
0.1	1	5	4	50	0.001 – 0.1	0 – 100
0.1	1	10	0.2	100	0.001 – 0.4	0 – 100
0.1	1	15	0.05	150	0.001 – 1.0	0 – 100
0.1	1.5	5	4	75	0.001 – 0.1	0 – 100
0.1	1.5	10	0.2	150	0.001 – 0.4	0 – 100
0.1	1.5	15	0.05	225	0.001 – 1.0	0 – 100

Varying parameters for simulations include the maximum growth rate, μ_0, light limiting depth, h_L, the critical depth, h_c, the windstress, τ_{wind}, and the surface heat flux, Q_0. The corresponding chlorophyll (Chl) concentration for each h_L value is noted in the table. The windstress is described as a range with a spacing of 0.001 Pa. The surface heat flux also covers a range. The spacing used is 5 W m^{-2}. The simulations in the top section are compared directly with LES results. The simulations on the bottom section are used for testing the sensitivity of μ_0 and h_L on the solution.

The resulting normalized net growth rate from the analytical model, $\sigma^* = \max(\sigma_n/m)$, is shown as a function of surface windstress and surface heat flux in Figures 10 and 11. The $\sigma^* = 0$ curve separates growing and decaying solutions and indicates the critical windstress for a given heat flux. In general, the normalized growth curves show that increasing the surface windstress leads to slower growth rates and that increasing surface heating promotes faster growth, as expected. Figure 10 shows contours of the growth rate for $h_c = 50$ m (corresponding to $h_L = 5$ m), whereas Figure 11 uses $h_c = 100$ m (corresponding to $h_L = 10$ m). When $Q_0 = 0$, the model predicts a critical windstress of ∼0.03 Pa when $h_L = 5$ m, whereas a higher critical windstress (∼0.13 Pa) is predicted when $h_L = 10$ m.

For comparison, symbols also indicate whether a specific LES exhibited growth (filled circle) or decay (open square) of phytoplankton concentration averaged over L for a given surface windstress and a heat flux. In general, the $\sigma^* = 0$ contour predicted from the analytical model delineates the growing and decaying cases from the LES. However, when $Q_0 = 0$, the critical windstress is somewhat overpredicted by the model.

One interpretation of the critical depth hypothesis is that net phytoplankton growth should occur when the mixing depth is shallower than the critical depth. When the mixing depth is equal to the critical depth, $L = h_c$, no growth should occur. We can evaluate this hypothesis using the analytical model which includes the effects of limited turbulent mixing by comparing the $L = h_c$ contour with the $\sigma^* = 0$ contour, as shown in Figure 10a. In this case, the critical depth is $h_c = 50$ m, and indeed, the $L = 50$ m contour follows the $\sigma^* = 0$ contour relatively closely. The discrepancy between the two can largely be explained by the slight overestimate of the mixing depth in the cases with $Q \neq 0$. Similarly, the $L = 100$ m contour closely coincides with the zero growth rate contour for the case $h_c = 100$ m (Figure 11a).

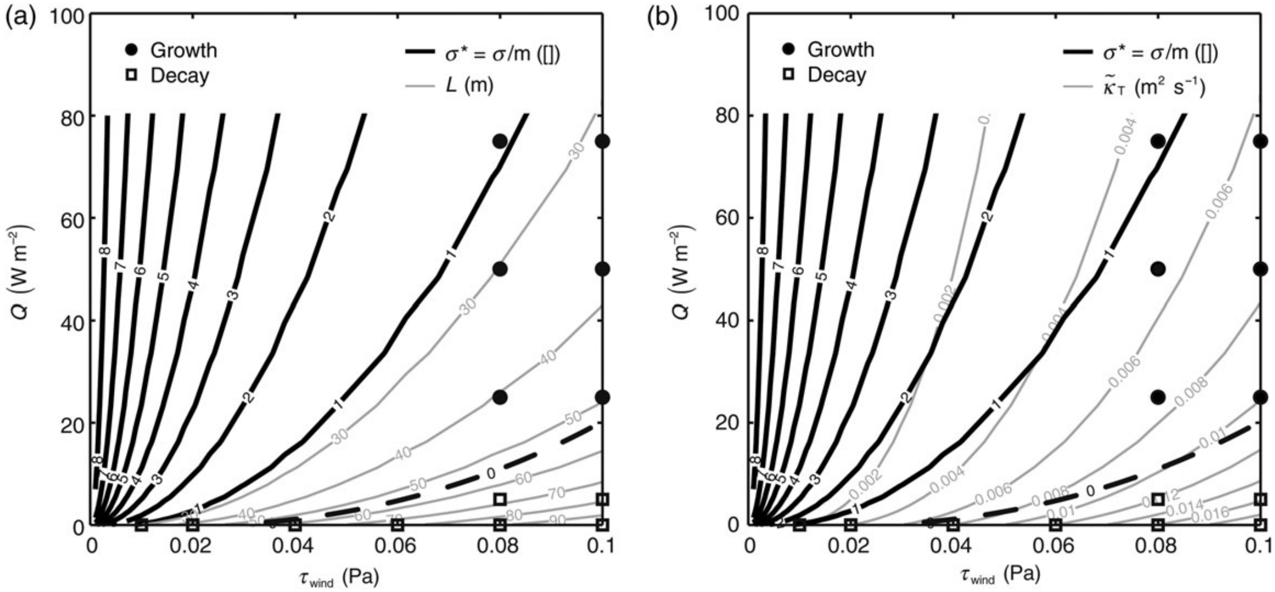

Figure 10. Normalized net growth rate, $\sigma^* \equiv \sigma/m$, curves from the analytical model as a function of the surface windstress, τ_{wind}, and surface heating, Q_0, with a critical depth, h_c, of 50 m (black). This critical depth corresponds to $h_L = 5$ m. The zero growth curve (dashed black lines) indicates the boundary between phytoplankton cell concentration growth and decay. The resulting growth (filled circle) or decay (open square) of phytoplankton cell concentration averaged over L from the LES is also shown. Contours of mixing depth, L (a), and phytoplankton turbulent diffusivity, $\tilde{\kappa}_T$ (b), are shown in grey.

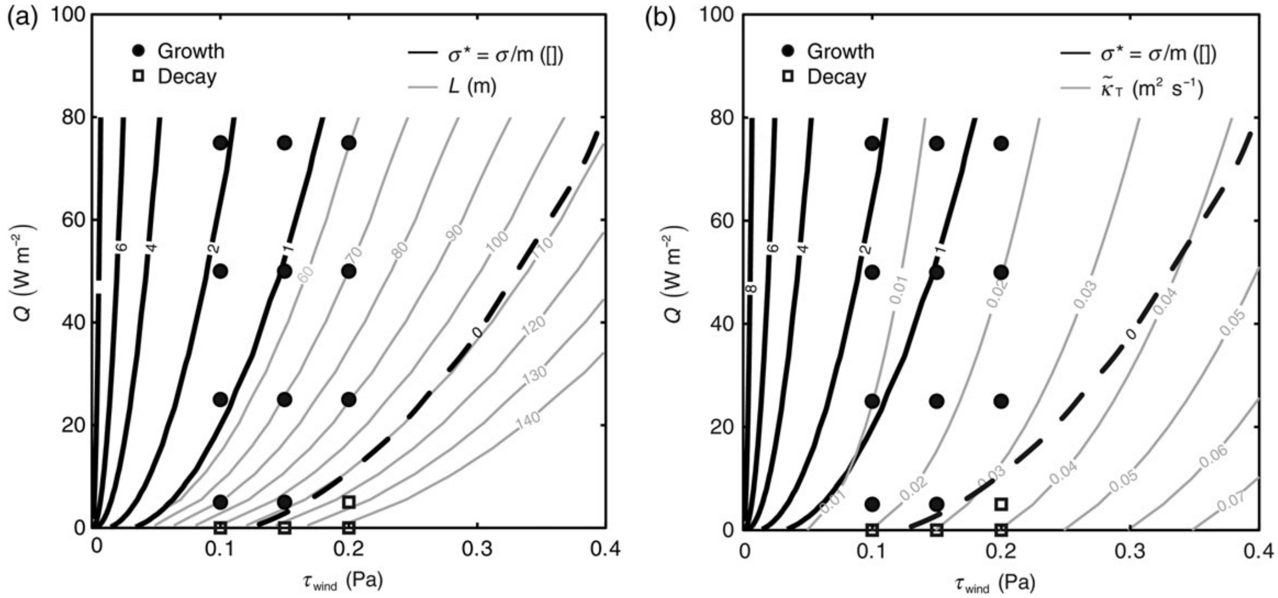

Figure 11. Same as Figure 10 but for $h_c = 100$ m (corresponding to $h_L = 10$ m). The scale of τ_{wind} is larger than Figure 10.

The magnitude of the turbulent diffusivity, estimated using Equations (16) and (17), is shown along with the growth rate contours in Figures 10b and 11b. To evaluate the critical turbulence hypothesis for a heated wind-driven boundary layer, we can compare the $\tilde{\kappa}_T = \kappa_c$ contour to the marginal stability contour ($\sigma^* = 0$). For $h_L = 5$ m, the critical turbulent diffusivity is $\kappa_c = 0.002$ m^2 s^{-1}, and the $\tilde{\kappa}_T = \kappa_c$ contour intersects the zero heat flux axis at ~0.01 Pa, which is less than the critical windstress ~0.03 Pa, predicted by the analytical model. For $h_L = 10$ m, the critical turbulent diffusivity is $\kappa_c = 0.009$ m^2 s^{-1}, and the $\tilde{\kappa}_T = \kappa_c$ contour intersects the zero heat flux axis below the critical windstress ~0.13 Pa predicted by the analytical model. When $Q_0 > 0$ the $\tilde{\kappa}_T = \kappa_c$ and $\sigma^* = 0$ contours diverge further, indicating that the critical turbulence becomes less significant with increased surface heating.

Analytical expressions for the critical windstress and the critical heat flux can be obtained by solving Equation (14) for a range of surface windstress and heat flux values. For a given surface windstress or a given surface heat flux, the corresponding critical surface condition can be estimated. To do this, we will use the approximate expression for the critical turbulent diffusivity from Equation (10) and substitute Equations (16) and (17) for the turbulent diffusivity. Without surface heating ($Q_0 = 0$), the critical windstress is

$$\frac{\tau_{crit}}{\rho_0} = \frac{f}{C_1 C_3} \frac{h_L^2}{m} (\mu_0 - m)^2. \tag{18}$$

When the surface heating and windstress are both non-zero, the analytical solutions are somewhat more complicated. The critical buoyancy flux is

$$B_{crit} = \left(\frac{\tau_{wind}}{\rho_0}\right)^3 \frac{C_2^2 C_3^2 m^2}{h_L^4 (\mu_0 - m)^4 f} - \left(\frac{\tau_{wind}}{\rho_0}\right) \frac{C_2^2 f}{C_1^2}. \tag{19}$$

From this expression, the critical surface heat flux can be calculated using $Q_{crit} = B_{crit} c_p \rho_0 / (\alpha g)$, where c_p and α are the heat capacity and thermal expansion coefficient, respectively. It is less simple to isolate an expression for the critical windstress with surface heating which satisfies the following cubic equation

$$C_3^2 m^2 \frac{\tau_{crit}}{\rho_0} = h_L^4 (\mu_0 - m)^4 \left(\frac{f^2 \rho_0}{C_1^2 \tau_{crit}} + \frac{\rho_0^2 f B_0}{C_2^2 \tau_{crit}^2} \right), \tag{20}$$

where B_0 is the surface buoyancy flux. This equation can be readily solved numerically, but the closed form expression for τ_{crit} is cumbersome. However, we can rewrite Equation (20) in terms of the Ekman layer depth, δ_{Ekman}, and the stable boundary layer depth, δ_{SBL}, defined in the "Mixing depth and turbulent diffusivity sales" section:

$$C_3^2 m^2 \frac{\tau_{crit}}{\rho_0} = h_L^4 (\mu_0 - m)^4 \left(\frac{1}{C_1^2 \delta_{Ekman}^2} + \frac{1}{C_2^2 \delta_{SBL}^2} \right). \tag{21}$$

Although δ_{Ekman} and δ_{SBL} both depend implicitly on the windstress, we can examine limits when one is much smaller than the other. When surface heating is small and $\delta_{Ekman} << \delta_{SBL}$, we recover the expression given in Equation (18). In the other limit, when heating is large enough to confine mixing to a depth much shallower than the Ekman depth, i.e. when $\delta_{SBL} << \delta_{Ekman}$, the critical windstress is

$$\frac{\tau_{crit}}{\rho_0} = \left(f B_0 h_L^4 \frac{(\mu_0 - m)^4}{m^2} \frac{C_2^2}{C_3^2} \right)^{1/3}. \tag{22}$$

Note that large stabilizing surface buoyancy fluxes increase the critical windstress. The critical windstress also depends strongly on h_L, μ_0, and m.

Numerical solutions of Equation (20) are shown in Figure 12 for various values of the critical depth. Each curve traces out solutions with no net growth as a function of the windstress and the surface heat flux. The figure can therefore be used to find the critical surface heat flux for a given windstress, or conversely the critical windstress for a given surface heat flux. We expand on the simulations presented above by adding an additional value of $h_L + 15$ m and allowing μ_0 to vary from 0.5, 1.0, and 1.5 d^{-1}. This causes the critical depth, h_c, to vary over a wide range from 25 to 225 m. Figure 12 shows that as the critical depth increases, the critical

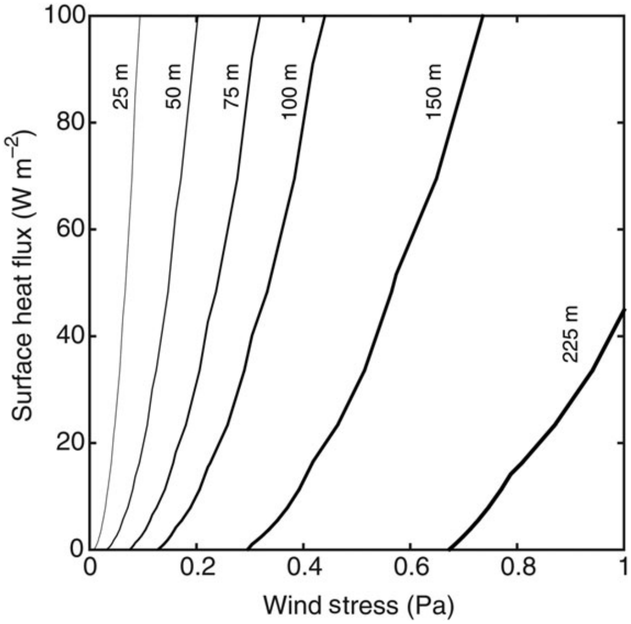

Figure 12. Normalized analytical critical growth, σ^*, curves as a function of the surface windstress and surface heat fluxes. These curves represent the sensitivity of the critical growth curve to the critical depth, $h_c = h_L(\mu_0/m)$. Each curve represents a solution for a given critical depth, which results from varying $\mu_0 = 0.5$, 1, and 1.5 d^{-1} and the *e*-folding depth associated with light penetration, $h_L = 5$, 10, and 15 *m*. The loss rate, *m*, is constant and is set to 0.1 d^{-1}. From right to left, the critical depths increase from 25 to 225 m, indicating that a higher critical depth requires a higher critical windstress for a given heat flux.

growth curve shifts towards higher windstresses and lower surface heat fluxes. In other words, a larger critical depth requires a stronger wind to suppress a bloom.

Discussion and conclusions

In this paper, LES were used to study the response of phytoplankton to wind-driven mixing and surface heating. Results from a series of LES runs forced with various constant values of the windstress and surface heat flux were used to develop parameterizations for the mixing depth and turbulent diffusivity and assess the analytical model that was based on these parameterizations. We then presented analytical solutions to extend the LES results to a wider range of parameter values and obtained expressions for the critical windstress and the critical heat flux in terms of other physical and biological parameters.

The LES results indicate that the depth and intensity of mixing are each capable of influencing phytoplankton growth. In the absence of positive heating averaged over a day, net phytoplankton growth occurs in the LES when the windstress is below a critical threshold. The LES results agree with the critical depth hypothesis; phytoplankton growth occurs when the mixing depth first becomes shallower than the critical depth. In this case, wind-driven mixing maintains a relatively uniform phytoplankton concentration in the mixing layer, and growth conditions are consistent with the critical depth hypothesis based on the mixing layer depth rather than the mixed layer depth. During this period, there is a decoupling between the mixed and the mixing layer.

The critical windstress predicted by our analytical model depends strongly on the surface heat flux and the critical depth (Figure 12). In the absence of heating and when the critical depth is relatively small ($h_c \leq 50$ m), the critical windstress is very small (<0.05 Pa). In this case, very little wind is sufficient to mix phytoplankton out of the euphotic layer and prevent a bloom. This is consistent with the conclusion drawn by Taylor and Ferrari (2011b) who found that very low levels of surface cooling were sufficient to prevent blooms. However, Figure 12 also shows that the critical windstress is highly sensitive to the critical depth. This is a new result and was not seen under convective conditions. Unlike convection which extends throughout the mixed layer, wind-driven mixing cannot extend far below the Ekman layer depth in the absence of surface heat fluxes. Therefore, a large windstress is required to keep phytoplankton cells well-mixed below a deep critical depth. The addition of surface heating strongly restricts the depth of mixing and results in a sharp increase in the critical windstress.

We can interpret the sensitivity of phytoplankton growth to winds and heating using the parameterizations for the mixing depth and turbulent diffusivity introduced in Equations (16) and (17). First, consider a case with no net heat flux ($Q_0 = 0$), where $L \propto u_*/f$ and $\kappa_T \propto u_*^2/f$. If the windstress is reduced by an amount $\Delta\tau_{\text{wind}}$, the mixing depth, L, will be reduced by a factor proportional to $\sqrt{\Delta\tau_{\text{wind}}}$, whereas the turbulent diffusivity, κ_T, will decrease by a factor of $\Delta\tau_{\text{wind}}$. Depending on the particular physical and biological conditions, it is therefore possible for κ_T to drop below the critical turbulence threshold before the mixing depth shoals above the critical depth. Conversely, when the mixing depth is strongly influenced by the stabilizing effect of surface heating and $L \propto u_*^2/\sqrt{B_0 f}$, an increase in the surface heat flux will reduce L and κ_T by the same factor. Therefore, if the turbulent diffusivity associated with wind-driven mixing alone is much larger than the critical turbulence threshold, it is unlikely that increasing the surface heating will trigger a bloom through the critical turbulence criterion before the mixing depth shoals above the critical depth.

In an effort to isolate the influence of various physical mechanisms on the timing of the spring bloom, we used a highly simplified phytoplankton model. We neglected several factors that could be important in the timing of the spring bloom, including phytoplankton/zooplankton interactions (Behrenfeld, 2010), nutrient availability (Moore *et al.*, 2006), and eddy-driven restratification (Taylor and Ferrari, 2011a; Mahadevan *et al.*, 2012). The results of our model are therefore best interpreted not as a prediction for the timing of a given bloom event, but rather an indication of the sensitivity of phytoplankton growth to winds and surface heating. Part of the rationale for considering a simplified phytoplankton model is that LES simulations are very costly, which makes exploring a vast parameter space extremely challenging. However, the analytical model that we presented could be expanded to include a more complex biogeochemical model and used to study how a complex ecosystem responds to changes in physical forcing.

Acknowledgements

We thank Stephanie Henson, Marina Lévy, Joan Llort, and Anna Rumyantseva for their helpful discussions on spring blooms. We would also like to express our gratitude to an anonymous reviewer for the many constructive critiques. This work was supported through a Newton International Fellowship from the Royal Society to RME. JRT was supported by a grant from the Natural Environment Research Council, award NE/J010472/1.

References

Basu, S., and Porté-Agel, F. 2006. Large-eddy simulation of stably stratified atmospheric boundary layer turbulence: a scale-dependent dynamic modeling approach. Journal of the Atmospheric Sciences, 63: 2074–2091.

Beare, R. J., Macvean, M. K., Holtslag, A. A. M., Cuxart, J., Esau, I., Golaz, J-C., Jimenez, M. A., *et al.* 2006. An intercomparison of large-eddy simulations of the stable boundary layer. Boundary-Layer Meteorology, 118: 247–272.

Behrenfeld, M. J. 2010. Abandoning Sverdrup's critical depth hypothesis on phytoplankton blooms. Ecology, 91: 977–989.

Boss, E., and Behrenfeld, M. 2010. In situ evaluation of the initiation of the North Atlantic phytoplankton bloom. Geophysical Research Letters, 37: 1–5.

Brainerd, K. E., and Gregg, M. C. 1995. Surface mixed and mixing layer depths. Deep Sea Research I: Oceanographic Research Papers, 42: 1521–1543.

Brody, S. R., and Lozier, M. S. 2014. Changes in dominant mixing length scales as a driver of subpolar phytoplankton bloom initiation in the North Atlantic. Geophysical Research Letters, 41: 3197–3203.

Brody, S. R., Lozier, M. S., and Dunne, J. P. 2013. A comparison of methods to determine phytoplankton bloom initiation. Journal of Geophysical Research: Oceans, 118: 2345–2357.

Broekhuizen, N. 1999. Simulating motile algae using a mixed Eulerian-Lagrangian approach: does motility promote dinoagellate persistence or co-existence with diatoms? Journal of Plankton Research, 21: 1191–1216.

Chiswell, S. M. 2011. Annual cycles and spring blooms in phytoplankton: don't abandon Sverdrup completely. Marine Ecology Progress Series, 443: 39–50.

Cullen, J. J., and Lewis, M. R. 1988. The kinetics of algal photoadaptation in the context of vertical mixing. Journal of Plankton Research, 10: 1039–1063.

Ebert, U., Arrayás, M., Temme, N., Sommeijer, B., and Huisman, J. 2001. Critical conditions for phytoplankton blooms. Bulletin of Mathematical Biology, 63: 1095–1124.

Enriquez, R. M. 2013. Subgrid-scale turbulence modeling for improved large-eddy simulation of the atmospheric boundary layer. PhD Dissertation, Stanford University, 207 pp.

Ferrari, R., Merrifield, S. T., and Taylor, J. R. 2014. Shutdown of convection triggers increase of surface chlorophyll. Journal of Marine Systems. doi:10.1016/j.jmarsys.2014.02.009.

Gran, H. H., and Braarud, T. 1935. A quantitative study of the phytoplankton in the Bay of Fundy and the Gulf of Maine (including observations on hydrography, chemistry and turbidity). Journal of the Biological Board of Canada, 1: 279–467.

Holte, J., and Talley, L. 2009. A new algorithm for finding mixed layer depths with applications to argo data and subantarctic mode water formation. Journal of Atmospheric and Oceanic Technology, 26: 1920–1939.

Huisman, J., van Oostveen, P., and Weissing, F. 1999. Critical depth and critical turbulence: two different mechanisms for the development of phytoplankton blooms. Limnology and Oceanography, 44: 1781–1787.

Kara, A. B., Rochford, P. A., and Hurlburt, H. E. 2000. An optimal definition for ocean mixed layer depth. Journal of Geophysical Research, 105: 16803.

Kosović, B., and Curry, J. A. 2000. A large eddy simulation study of a quasi-steady, stably stratified atmospheric boundary layer. Journal of the Atmospheric Sciences, 57: 1052–1068.

Lien, R -C., and Sanford, T. B. 2004. Turbulence spectra and local similarity scaling in a strongly stratified oceanic bottom boundary layer. Continental Shelf Research, 24: 375–392.

Lilly, D. K. 1992. A proposed modification of the Germano subgrid-scale closure method. Physics of Fluids A, 4: 633–635.

Mahadevan, A., D'Asaro, E., Lee, C., and Perry, M. J. 2012. Eddy-driven stratification initiates North Atlantic spring phytoplankton blooms. Science, 337: 54–58.

Mason, P. J., and Derbyshire, S. H. 1990. Large-eddy simulation of the stably-stratified atmospheric boundary layer. Boundary-Layer Meteorology, 53 (1–2): 117–162.

Moore, C. M., Mills, M. M., Milne, A., Langlois, R., Achterberg, E. P., Lochte, K., Geider, R. J., *et al.* 2006. Iron limits primary productivity during spring bloom development in the central North Atlantic. Global Change Biology, 12: 626–634.

Nagai, T., Yamazaki, H., and Kamykowski, D. 2004. A Lagrangian photoresponse model coupled with 2nd-order turbulence closure. Marine Ecology Progress Series, 265: 17–30.

Riley, G. A. 1946. Factors controlling phytoplankton populations on Georges Bank. Journal of Marine Research, 6: 54–73.

Ross, O. N., and Sharples, J. 2004. Recipe for 1-d Lagrangian particle tracking models in space-varying diffusivity. Limnology and Oceanography: Methods, 2: 289–302.

Sverdrup, H. 1953. On conditions for the vernal blooming of phytoplankton. Journal du Conseil International pour l'Exploration de la Mer, 18: 287–2985.

Taylor, J. R. 2008. Numerical simulations of the stratified oceanic bottom boundary layer. PhD Thesis, University of California, San Diego.

Taylor, J. R., and Ferrari, R. 2010. Buoyancy and wind-driven convection at mixed layer density fronts. Journal of Physical Oceanography, 40: 1222–1242.

Taylor, J. R., and Ferrari, R. 2011a. Ocean fronts trigger high latitude phytoplankton blooms. Geophysical Research Letters, 38: 1–5.

Taylor, J. R., and Ferrari, R. 2011b. Shutdown of turbulent convection as a new criterion for the onset of spring phytoplankton blooms. Limnology and Oceanography, 56: 2293–2307.

Taylor, J. R., and Sarkar, S. 2008. Direct and large eddy simulations of a bottom Ekman layer under an external stratification. International Journal of Heat and Fluid Flow, 29: 721–732.

Townsend, D. W., Cammen, L. M., Holligan, P. M., Campbell, D. E., and Pettigrew, N. R. 1994. Causes and consequences of variability in the timing of spring phytoplankton blooms. Deep Sea Research I: Oceanographic Research Papers, 41: 747–765.

Wyngaard, J. C. 2010. Turbulence in the Atmosphere. Cambridge University Press, New York. 393 pp.

Yamazaki, H., Locke, C., Umlauf, L., Burchard, H., Ishimaru, T., and Kamykowski, D. 2014. A Lagrangian model for phototaxis-induced thin layer formation. Deep Sea Research II: Topical Studies in Oceanography, 101: 193–206.

Zhou, B., and Chow, F. K. 2011. Large-eddy simulation of the stable boundary layer with explicit filtering and reconstruction turbulence modeling. Journal of the Atmospheric Sciences, 68: 2142–2155.

Zhou, B., and Chow, F. K. 2012. Turbulence modeling for the stable atmospheric boundary layer and implications for wind energy. Flow, Turbulence and Combustion, 88: 255–277.

Zikanov, O., Slinn, D. N., and Dhanak, M. R. 2003. Large-eddy simulations of the wind-induced turbulent Ekman layer. Journal of Fluid Mechanics, 495: 343–368.

Zilitinkevich, S., and Baklanov, A. 2002. Diagnostic and prognostic equations for the depth of the stably stratified Ekman boundary layer. Quarterly Journal of the Royal Meteorological Society, 128: 25–46.

Zilitinkevich, S., Esau, I., and Baklanov, A. 2007. Further comments on the equilibrium height of neutral and stable planetary boundary layers. Quarterly Journal of the Royal Meteorological Society, 133: 265–271.

Zilitinkevich, S. S. 1972. On the determination of the height of the Ekman boundary layer. Boundary-Layer Meteorology, 3: 141–145.

Appendix

Comparison of LES and analytical model results

In this section, we compare the calculated mixing depth and phytoplankton growth rate results from the LES and analytical model to understand any model biases.

The values of the mixing depth from the analytical model and the LES are shown in Figure A1. The analytical model underpredicts the mixing depth for the unheated cases and slightly overpredicts the mixing depth for the heated cases. This is because the coefficient C_1 in Equation (16) tended to be higher than the chosen value for the

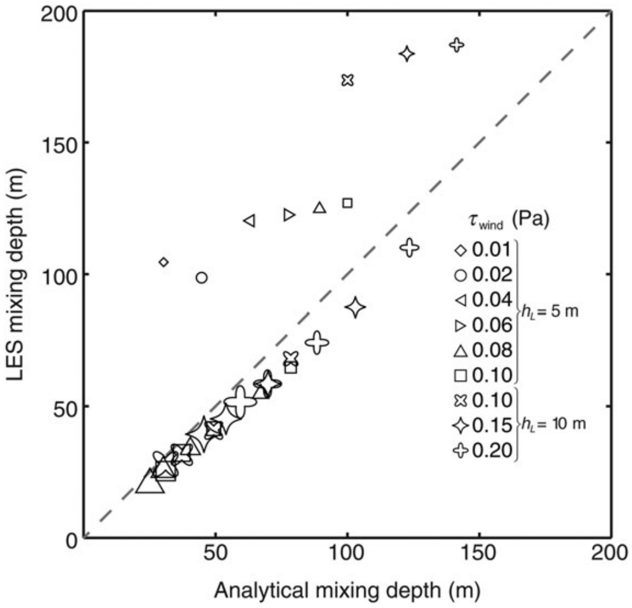

Figure A1. Comparison of mixing depths from LES and analytical solutions for various windstress, τ_{wind}, and surface heating, Q_0, cases. Symbols depict individual values of τ_{wind}. Larger symbols indicate higher levels of Q_0.

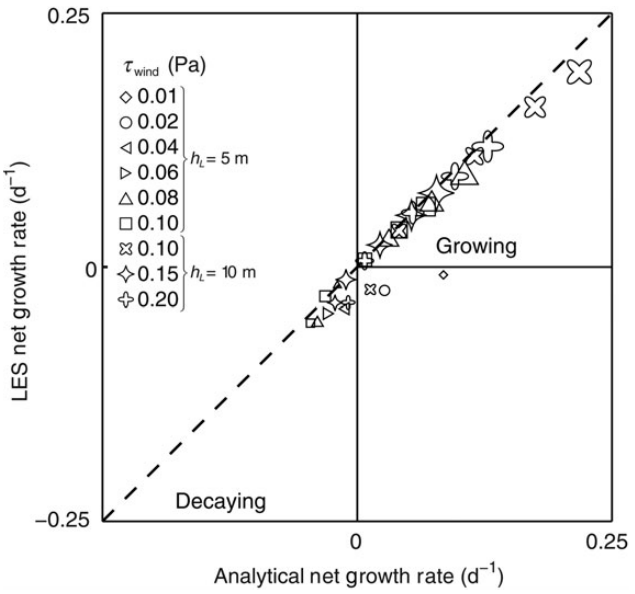

Figure A2. Comparison of net growth rates from LES and analytical solutions for various windstress, τ_{wind}, and surface heating, Q_0, cases. Symbols depict individual values of τ_{wind}. Larger symbols indicate higher levels of Q_0.

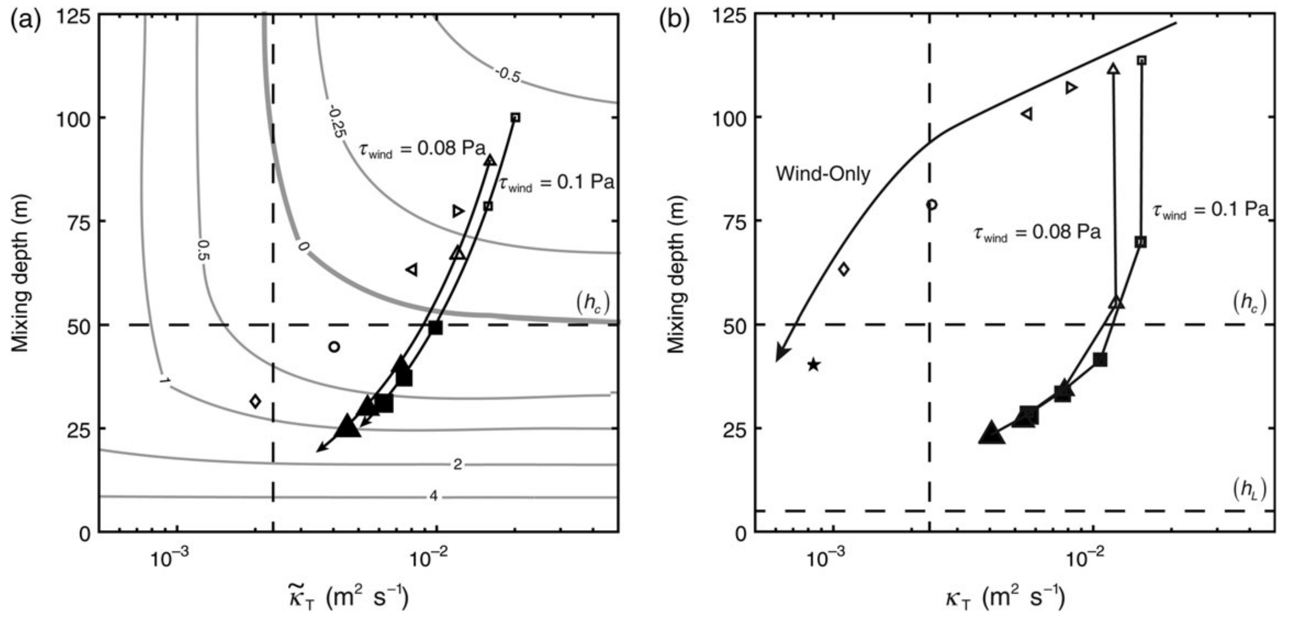

Figure A3. Normalized analytical growth, σ^*, curves (grey) as a function of the turbulent diffusivity, $\tilde{\kappa}_T$, and mixing depth, L (a). Arrows indicate the movement from an unheated case to higher surface heating, Q_0, cases for a given τ_{wind}. The mixing depth and turbulent diffusivity from the LES are shown in (b). Lines connect the cases with the same τ_{wind}. Dashed lines indicate the critical turbulent diffusivity, κ_c, and the critical depth, h_c. Symbols depict individual values of τ_{wind}: star, 0.001 Pa; diamond, 0.01 Pa; circle, 0.02 Pa; left-pointing pointer, 0.04 Pa; right-pointing pointer, 0.06 Pa; triangle, 0.08 Pa; square, 0.10 Pa. Filled symbols correspond to phytoplankton cell concentration growth.

wind-only cases. Rather than using distinct values of the coefficients in the heated and unheated cases, we chose a combination of C_1 and C_2 that led to the smallest standard deviation in the normalized eddy diffusivity profiles across all cases.

Figure A2 shows a comparison of the growth rates from the analytical model and the LES. Overall, the analytical model captures the growth rate inferred from the LES well, although there are some differences, notably in the unheated case with $\tau_{\rm wind} = 0.01$ Pa. For this case, the model predicts significant phytoplankton growth, but the LES shows weak decay for the period examined, although the growth rates are small in magnitude in both models. The overprediction of the growth rates from the analytical model when $Q_0 = 0$ appears to be due to an underestimate in the mixing depth for these cases.

Figure A3 shows contours of the normalized growth rate from the analytical model (σ^*) as a function of $\kappa_{\rm T}$ and L for the cases with $h_{\rm L} = 5$ m (corresponding to $h_{\rm c} = 50$ m). The critical turbulent diffusivity and critical depth thresholds are depicted as dashed lines. Symbols indicate the values of the turbulent diffusivity and mixing depth calculated for the analytical model with values of Q and $\tau_{\rm wind}$ corresponding to each LES run. Arrows indicate the direction of increasing surface heat flux, Q_0, for a constant windstress, $\tau_{\rm wind}$. When following along a series with $\tau_{\rm wind} = 0.08$ or 0.1 Pa, and increasing the surface heat flux, the trajectory crosses the $\sigma^* = 0$ contour when the mixing depth is very close to the critical depth.

The turbulent diffusivity and mixing depth diagnosed directly from the LES with $h_{\rm L} = 5$ m (corresponding to $h_{\rm c} = 50$ m) are shown in Figure A3. Comparing Figure A3, it is clear that the model significantly underpredicts L for the cases with $Q_0 = 0$. However, the turbulent diffusivity from the analytical model matches the turbulent diffusivity diagnosed from the LES more closely. The coefficients for the analytical model were selected to predict the eddy diffusivity more accurately than the mixing depth. Additionally, there is more disagreement in the normalized eddy diffusivity profiles for the unheated cases than the heated cases. Therefore, it is also expected that there would be more agreement between the analytical model and LES eddy diffusivities for the heated cases. Following the series with $Q_0 = 0$ in Figure A3 from high to low windstress, growth does not begin when the critical turbulence threshold is crossed. The LES also demonstrates that phytoplankton growth occurs when the mixing depth is less than the critical depth. To see this trajectory, we add a special $\tau_{\rm wind} = 0.001$ Pa wind-only case to this figure.

The results shown are for cases with $h_{\rm c} = 50$ m. However, the results are qualitatively similar for the cases with $h_{\rm c} = 100$ m. By comparing Figures 10 and 11, we see that higher values of windstress are needed to suppress growth for deeper critical depths. The analytical model and LES results for the cases with $h_{\rm c} = 100$ m also show that phytoplankton growth occurs when the mixing depth is less than the critical depth.

Handling editor: Shubha Sathyendranath